Journal of Alloys and Compounds 869 (2021) 159268

Contents lists available at ScienceDirect

Journal of Alloys and Compounds

journal homepage: www.elsevier.com/locate/jalcom

Investigation of microstructure and hydrogen absorption properties of bulk immiscible AgRh alloy nanoparticles

Akhil Tayal[a,*,1], Okkyun Seo[b,1], Jaemyung Kim[b], Kohei Kusada[c], Hirokazu Kobayashi[c], Hiroshi Kitagawa[c], Osami Sakata[b,d,e,**]

[a] Deutsches Elektronen-Synchrotron, Notkestrasse 85, 22607 Hamburg, Germany
[b] Synchrotron X-ray Group, Research Center for Advanced Measurement and Characterization, National Institute for Materials Science, 1-1-1 Kouto, Sayo, Hyogo 679-5148, Japan
[c] Division of Chemistry, Graduate School of Science, Kyoto University, Kitashirakawa Oiwake-cho, Sakyo-ku, Kyoto 606-8502, Japan
[d] Department of Materials Science and Engineering, Tokyo Institute of Technology, Nagatsuta, Midori, Yokohama 226-8502, Japan
[e] Center for Synchrotron Radiation Research, Japan Synchrotron Radiation Research Institute (JASRI), 1-1-1 Kouto, Sayo, Hyogo 679-5198, Japan

ARTICLE INFO

Article history:
Received 18 December 2020
Received in revised form 13 February 2021
Accepted 17 February 2021
Available online 19 February 2021

Keywords:
Ag-Rh alloy nanoparticles
XAFS
Hydrogen absorption
Heterogeneous alloy

ABSTRACT

Bimetallic alloy nanoparticles (NPs) exhibit superior catalytic and chemical storage properties relative to the monometallic NPs. Previously, it has been reported that bimetallic AgRh forms solid-solution alloy NPs that have unusual hydrogen storage properties not commonly observed in individual Ag and Rh NPs. Here, we use a combination of X-ray diffraction (XRD) and X-ray absorption fine structure spectroscopy (XAFS) techniques to investigate the microstructure and unique hydrogen absorption properties of bulk immiscible AgRh alloy NPs. XRD analysis reveals that the long-range structure of the alloy sample can be estimated as a single fcc phase with a slightly smaller lattice parameter than that of the bulk Ag and larger than that of bulk Rh. XAFS analysis reveals that charge transfer between Rh and Ag occurs in this interfacial region. The near-edge profile reveals a variety of local environments for Ag and Rh, including distinct atomic pair distances and disorder. The atomic pair distances were compressed around Ag and elongated around Rh. A substantial fraction of the sample is an alloy phase formed by mixing of nano/sub-nanosized domains of Rh and Ag NPs. Mixing at the atomic level mainly occurs in the interfacial region. Consequently, the interfacial region has an important influence over the microstructure and provides active sites for hydrogen absorption.

1. Introduction

Nanoparticles (NPs) of noble metals are widely used in catalytic and chemical storage applications. These materials have unique properties that can be attributed to their electronic structure and density of states at the Fermi level [1]. Many previous investigations have revealed that the performance of noble metal NPs can further be improved using oxide supports and by optimizing the particle size and crystallographic faces taking part in the catalytic process. The catalytic performance of NPs dispersed on oxide supports has been observed to vary markedly with NP size, shape, the nature of the oxide support, and interactions between these components [2]. Similarly, catalytic properties are substantially influenced by the microstructure, which strongly depends on the size and shape of the NPs. Catalytic activity varies considerably at different crystallographic faces taking part in the catalytic process [3]. These findings highlight the importance of the interfacial structure between the NPs and the oxide-support and the microstructure of the system, which in turn are related to the NP size, shape, and inhomogeneity. Therefore, comprehensive knowledge of the interfacial structure and microstructure is required to understand the catalytic properties of alloy NPs fully.

It has been frequently reported that the performance of monometallic nanoparticles is limited under certain operating conditions. The limitations of monometallic NPs, in terms of site activities and selectivities, can be improved using bimetallic NPs catalysts [4–7]. Recently, bimetallic NPs, such as Pd-Ru [8–10], Ru-Cu [11], Pt-Ru [12,13], Au-Pt [14,15], Ag-Au [16,17], Ag-Rh [7, 18–26],

* Corresponding author.
** Corresponding author at: Synchrotron X-ray Group, Research Center for Advanced Measurement and Characterization, National Institute for Materials Science, 1-1-1 Kouto, Sayo, Hyogo 679-5148, Japan.
E-mail addresses: akhil.tayal@desy.de (A. Tayal), SAKATA.Osami@nims.go.jp (O. Sakata).
[1] Authors contributed equally to this work.

https://doi.org/10.1016/j.jallcom.2021.159268
0925-8388/

Au-Ir [27], and Au-Ru [28] have shown better catalytic performance, hydrogen storage capacity, and thermal stability [29,30] compared with those properties of monometallic NP systems. Notably, many of these bimetallic systems are immiscible in a bulk form. The formation of a solid-solution phase only occurs in the nanoparticles and is facilitated by thermodynamic behaviors unique to nano-sized systems. Therefore, novel electronic properties and microstructures emerge around the interfacial regions of these bulk immiscible NP systems, which have notable effects on the catalytic properties. These bimetallic systems suffer from thermodynamical instability owing to their immiscible nature and can therefore segregate to form isolated clusters in alloy NPs. The transformation from a metastable to a stable phase can readily occur if enough activation energy is provided in the form of heat, perturbations in the catalytic process, or structural disorder. Therefore, the observed catalytic properties in these systems cannot be fully understood in terms of their novel electronic properties and the role of their microstructure is equally important. In this regard, it is essential to investigate the structure of these materials at the interfacial region to gain a better understanding of their catalytic and chemical storage properties. Such investigations will also realize new materials by the engineering of the microstructure and interfacial structure.

X-ray absorption fine structure (XAFS) analysis is a well-known technique that can provide local structural information around both elements in bimetallic systems through its elemental selectivity. Here, we use XAFS to investigate AgRh alloy NPs in the ambient and in-situ hydrogen absorption conditions. We examined the local structure around Ag and Rh to understand the role of the interfacial structure on the H_2 absorption properties. Bimetallic alloy Rh NP catalysts are widely used to reduce nitrogen oxides with hydrocarbons [18]. Kotsifa et al. observed that this process is sensitive to the operating temperature and depends strongly on the physiochemistry and type of noble metal catalyst and oxide support [18]. Obuchi et al. found that Rh is highly selective for the formation of N_2 relative to N_2O in the NO_x reduction process compared with other metals such as Pt, Pd, Ru, and Ir [31]. The performance of Rh NPs improves markedly for an Al_2O_3 support compared with other oxide supports [32]. These findings reveal that reduction of NO_x with a hydrocarbon is a structurally sensitive process that is influenced by the interfacial structure between the Rh and oxide support and unique interactions offered by the different physiochemistry of NPs having distinct microstructures [18]. Recently, it has been shown that AgRh bimetallic alloys have hydrogen storage properties [21]. Notably, neither Rh nor Ag have any hydrogen storage properties in their monometallic form. This result suggests that in a bimetallic alloy, such as AgRh, unique structural properties in the interfacial region may promote unusual catalytic properties.

Many studies have been conducted on the AgRh systems with an emphasis on their synthesis methods [7,19,23]. Observations of superior catalytic and unconventional H_2 storage properties are generally attributed to charge transfer from Rh to Ag, which makes it more electropositive and enhances the NO_x reduction [20]. Seo et al. observed that the addition of Ag increases the NO bond energy, and improves the catalytic performance towards NO_x reduction [33]. Yang et al. observed that hybridization between the Ag and Rh electronic states causes the valence band of AgRh alloys to match well with that of Pd, which is a well-known material for the hydrogen storage, suggesting potential for AgRh to show hydrogen storage properties [22]. However, the structural aspects of this alloy and their effects on the observed hydrogen storage and catalytic performance remain poorly understood. In this report, we used a combination of XRD and XAFS techniques to investigate the microstructure of AgRh alloys. Furthermore, we performed in-situ XAFS measurements under H_2 to reveal the role of the interfacial structure on the observed hydrogen storage properties.

2. Experimental

The XAFS measurements were performed at the P64 beamline of DESY, Hamburg [34]. The NPs samples were filled into a 1-mm diameter capillary to perform measurements in transmission geometry. The open-ended capillary was mounted onto a reactor that allowed the gas to flow around the sample. During the XAFS data accumulation, either He or pure H_2 flowed under ambient temperature and pressure conditions. XAFS spectra were collected at the Ag K-edge and Rh K-edge. Normalization and background-subtraction of the data were performed with the use of the Athena software, and a standard procedure was followed [35]. The fitting of the extended X-ray absorption fine structure (EXAFS) data was performed using a computer code written by Conradson et al. [36]. The phase shift and photoelectron backscattering amplitude were theoretically calculated with the use of the Feff9 program [37]. The log-ratio analysis was performed in the Athena software [35].

The powder X-ray diffraction measurements were performed at the BL15XU NIMS beamline at SPring-8 in Japan. The synchrotron X-ray beam energy was selected at 29.195 keV using a Si (311) monochromator with an undulator. For the diffraction measurements, AgRh NPs were placed in a Lindemann glass capillary with an inner diameter of 0.2 mm. The X-ray diffraction signal was recorded with a CdTe detector (XR-100CdTe, AMPTEK, Inc.) in transmission geometry under a He gas atmosphere at room temperature.

AgRh alloy NPs with a poly(N-vinyl-2-pyrrolidone) (PVP) coating were synthesized by a chemical reduction method. The metal precursors of $AgNO_3$ and $Rh(CH_3COO)_3$ in a molar ratio of 50:50 were dissolved in water. The metal precursor solution was injected into ethylene glycol (EG) solution containing PVP at 170 °C. The AgRh alloy NPs were separated by centrifugation at room temperature. The average particle size of the AgRh alloy NPs was 12.2 ± 1.6 nm, as estimated by transmission electron microscope (TEM) imaging (Fig. S1).

3. Results and discussion

3.1. X-ray diffraction

Fig. 1 shows the powder X-ray diffraction pattern (Black open circle) of AgRh alloy NPs. The powder X-ray diffraction pattern was analyzed by the Rietveld refinement method (red line). The data were fitted assuming a single fcc crystal structure, indicating that the Ag-Rh alloys formed solid-solution alloy NPs. The lattice constant obtained from the peak positions (black marks) was 4.015 ± 0.003 Å. For reference, the lattice constants of bulk Ag and Rh are 4.08 and 3.803 Å, respectively, which suggests that alloy formation shifts the value of the average lattice parameter from the bulk values of Ag and Rh. The crystalline domain size of AgRh NPs was 4.8 ± 0.6 nm, as determined by the Debye–Scherrer equation: $D = K\lambda/2\Delta cos\theta$, where D is the crystalline domain size, K is the shape factor (0.9 for nanoparticles with the spherical shape), λ is the X-ray wavelength (λ = 0.4247 Å), Δ is the full width at half maximum in radians, and θ is the Bragg angle. Notably, the particle size obtained by TEM imaging was approximately 12 nm which is larger than the crystallite size obtained from diffraction analysis. This smaller apparent crystallite size implies that within the NPs, either multiple domains of smaller crystallites are present, or the alloy sample might contain a substantial fraction of non-crystalline or sub-nanometer size domains, which are not able to diffract coherently and hence have no XRD signal.

3.2. X-ray absorption near edge structure

Fig. 2 compare the X-ray absorption near edge structure (XANES) profiles for AgRh alloy NPs with Ag and Rh foil of high purity

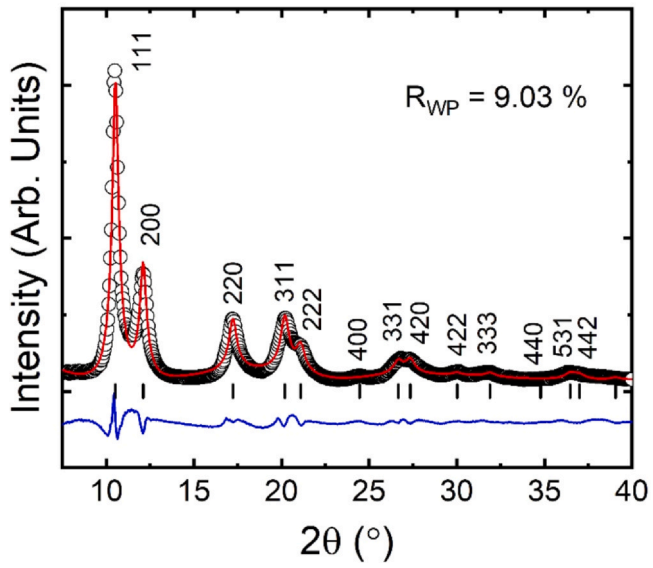

Fig. 1. Rietveld refinement of the XRD data measured on AgRh alloy NPs under ambient conditions.

measured at the Ag K-edge and Rh K-edge. The XANES spectra of both edges have two near-edge features marked by A and B in Fig. 2(a,b). The Rh K-edge spectra show that the energy separation between the near-edge features (A-B) decreased in the alloy sample compared with those of reference Rh foil. The opposite behavior was observed in the spectra measured at the Ag K-edge, where the separation between the features A and B was slightly greater for the alloy sample than for the bulk reference foil. In general, the near edge features A and B are attributed to the transition from *s* to *p* and

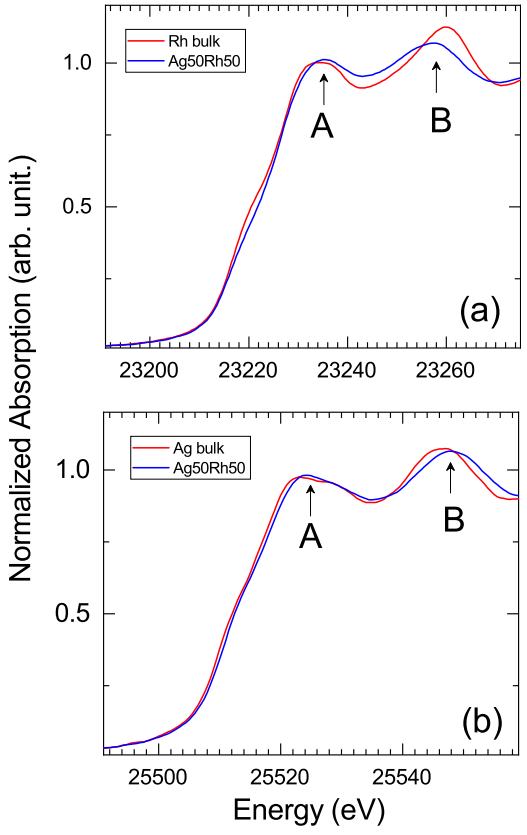

Fig. 2. XANES profiles of AgRh alloy NPs and bulk references measured at Rh K-edge (a) and Ag K-edge (b).

s to *f* states, respectively [38,39]. In literature, it has been argued that these features have a contribution from photoelectron backscattering, similar to the observation in the EXAFS [40]. Consequently, the separation between these features is found to follow an inverse relationship with the square of the atomic pair distance [40]. Therefore, the XANES results indicate that the atomic pair distances surrounding Rh in the AgRh alloy NPs are larger than those observed in bulk Rh. Similarly, the atomic pair distances around Ag are shorter in the alloy sample relative to those in bulk Ag. In a perfect solid-solution alloy with mixing at the atomic level, the atomic pair distances are expected to be similar surrounding both the Rh and Ag environments. Therefore, the observed distinct atomic pair distances around Ag and Rh suggest that rather than perfect atomic-level mixing, in alloy NPs, nano or sub-nanosized clusters of Ag and Rh are homogeneously mixed to form a nano solid-solution alloy phase.

However, the presence of an atomically mixed AgRh alloy phase cannot be completely ruled out. We considered that opposing changes in the atomic pair distance occur around Rh and Ag sites. Furthermore, a substantial shift in the atomic pair distance relative to the respective bulk phase was observed. Therefore, an interfacial region develops between homogeneously distributed nano or sub-nanosized clusters of Rh, and Ag can host AgRh alloy phase mixing at the atomic level. Owing to mixing at the atomic level, the interfacial region can propagate the epitaxial strain to nearby clusters and is capable of modifying the average long and short-range structure around both Ag and Rh, as observed from the XRD and XANES analysis. Therefore, the presence of an atomically mixed AgRh alloy phase in the sample cannot be neglected. This phase may be present in the form of a minority phase whose weighted contribution to the EXAFS signal is marginal. However, its effect on the long and short-range structure can be indirectly seen in the XRD and XANES data.

Now, if we consider the probe limitations of XRD and XAFS for the AgRh system. We know that Ag and Rh are close in the periodic table and have similar X-ray scattering lengths. Therefore it is difficult to distinguish between Ag and Rh atomic sites by diffraction techniques. Moreover, these techniques provide volume-average information and therefore provide the average values of the lattice parameters of the bulk sample. Importantly, sub-nanosized domains may have a disordered structure with domain sizes well below the diffraction limit that remains obscured by the XRD signal. Because of these limitations, information such as distinct atomic pair distances around Ag and Rh and any disordered domains cannot be obtained from XRD data. However, XAFS analysis is sensitive for probing the local structure and due to its elemental selectivity, any site-specific departure in the local structure from the average long-range structure can easily be assessed. The only caveat to this approach is that the photoelectron backscattering amplitudes of Rh and Ag are very similar; therefore, it is not possible to distinguish between mono- and bimetallic atomic pairs.

It has been reported that charge transfer from Rh to Ag is possible in an AgRh alloy [20,33]. On comparing the edge position (Fig. 2(a,b)), it can be seen that spectra measured at both edges for the alloy sample are shifted to higher energy, ruling out the possibility of any charge transfer between Ag and Rh. However, as discussed earlier, the XAFS provides information on the weight fraction of a particular component in the sample. The absence of a signature of charge transfer indicates that such alloying components are not the main phase in the sample. Such an alloying phase is likely to result from intermixing at the atomic level, which allows for hybridization between Ag and Rh electronic states. Therefore, alloy mixing at the atomic level is likely possible in the interfacial region between the sub-nanometer clusters of Ag and Rh. Because the rest of the phase will dominate the XAFS signal, contributions from the atomically mixed alloying component are minimal, preventing the observation of charge transfer between Ag and Rh in the XANES signal. Also, a small positive shift in the edge energy owing to

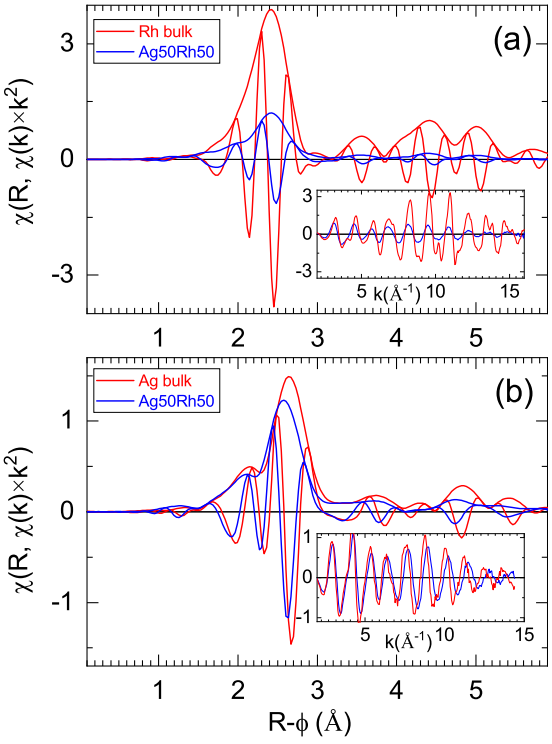

Fig. 3. Fourier transform (χ(R)) spectra of indicated samples measured at the Rh K-edge (a) and Ag K-edge (b) under ambient conditions. Inset of the figures show EXAFS (χ(k)k^2) spectra.

surface oxidation of the NPs may suppress any signs of charge transfer in the XANES spectra.

3.3. Extended X-ray absorption fine structure

A further comparison of the local structure around Rh and Ag was performed with a detailed analysis of the EXAFS data. Fig. 3(a,b) shows Fourier transform (χ(R)) and EXAFS (χ(k)k^2) spectra measured at the Rh K-edge and Ag K-edge for the alloy NPs and a reference sample under a constant He flow. On comparing the Ag K-edge χ(k) spectra of the AgRh sample with that of the bulk Ag, we deduced that the FT peaks and node position of the real component spectrum of AgRh sample shifted to a lower value than that of bulk Ag indicating a reduction in the Ag-Ag/Rh atomic pair distance. Moreover, a decrease in the FT amplitude for the first and higher-order peaks suggested that the sample is nanocrystalline, and contributions to the EXAFS signal from surface atoms having a lower coordination number are relatively high as is commonly observed in NP systems [41–43]. This behavior results in the appearance of a lower coordination number in the NPs sample relative to the bulk. Such a reduction in the FT amplitude can also correlate with the disorder [41,42,44,45]. However, a lower coordination number and higher disorder will affect the χ(k) amplitude differently across the k-region [41]. A smaller coordination reduces the χ(k) amplitude over the entire *k*-range. In contrast, the reduction in the χ(k) amplitude owing to higher disorder is greater in the high k-region. On comparing the χ(k) spectra of a sample measured at ambient temperature with respective bulk foils (Fig. 3 insets), we deduced that the χ(k) amplitude is smaller over the entire k-region for the AgRh sample, implying that the decrease of the FT peak amplitude is primarily attributed to the lower coordination number.

Notably, for the AgRh sample measured at the Rh K-edge, the decreases in the χ(k) and FT amplitude were much more significant than those of the bulk Rh. A similar decrease in the amplitude was not observed for the spectra measured at the Ag K-edge. These observations suggest that Rh forms smaller clusters than does Ag. However, the structural disorder also contributes to the reduction in the FT and χ(k) amplitude, as will be discussed later. The node position in the FT spectrum of the alloy sample is nearly identical to that of the bulk spectrum. However, the above Rh K-edge XANES analysis of the AgRh sample and Rh foil reveals that the separation between the near-edge features A and B is significantly different in both samples. Such differences in the near-edge features indicate that the atomic pair distances around Rh are different in the bulk and AgRh samples. Notably, XANES is less sensitive to disorder and anharmonicity caused by the non-Gaussian distribution of atomic pair distances [46–48]. Therefore, these parameters have a more significant contribution to the EXAFS signal than to the XANES signal, which results in the observed discrepancy between the XANES and EXAFS data. As pointed out earlier, TEM measurements of the AgRh alloy sample suggested that the bimetallic NPs were uniform in size at approximately 12 nm. However, the crystallite size determined from the XRD data was approximately 4.8 nm suggesting that the alloy NP sample had a large fraction of non-crystalline or nanosized domains, as expected for a metastable bimetallic alloy system. Any non-crystalline domains could be a source of disorder and contribute to structural anharmonicity.

The effects of anharmonicity in the sample were evaluated by incorporating higher-order cumulants viz. the third and fourth in the EXAFS analysis [42,44,45,48]. However, owing to parameter correlation, the third cumulant correlates with the atomic pair distance and the fourth cumulant correlates with the FT amplitude [49]. For spectra measured at the Rh K-edge, a negligible difference in the FT node positions and measurable changes in the near-edge features indicated that the higher-order cumulants have effects in the sample. Higher-order cumulants might correlate with the atomic pair distances and may contribute to the inconsistent atomic pair distances observed by XANES and EXAFS analysis. A contribution from higher-order cumulants may also be attributed to the markedly smaller FT and χ(k) amplitude for the spectrum measured at the Rh K-edge. The analysis of FT and χ(k) spectra measured at the Ag and Rh K-edge, however, confirmed that the contribution from structural anharmonicity is higher in the local environment of Rh and is relatively small or negligible for Ag. Additionally, the nano-sized clusters of Rh might be smaller than those of Ag. However, to obtain more precise information, we performed further analysis as discussed below.

In the light of possible correlations among various parameters in the EXAFS equation, first, we considered the effect of individual parameters on the EXAFS data. It is helpful before approaching the EXAFS fitting to estimate the metrical parameters. In this way, any ambiguity in the data interpretation owing to parameter correlation can be avoided. Various parameters, which are correlated in the equation defining χ(k), can be grouped together. It has been proposed that parameters having a high correlation among them are as follows. In the first group; R, c_3, and ΔE_0 viz. atomic pair distance, third cumulant, and relative variation in edge position and in the second group; σ, N, and S_0^2 viz. root mean square relative displacement, coordination number, and passive electron reduction factor, have high correlations among them. Therefore, in the case of different degrees of disorder, anharmonicity, and distinct atomic pair distances, the fitting model used to obtain metrical parameters may not be unique and will have a certain ambiguity. In this regard, a prior knowledge of certain parameters that strongly affect the EXAFS results would be helpful in constraining the correlated parameters during the EXAFS fitting. Moreover, it can also be useful to assess the effects of individual parameters on the raw EXAFS signal.

It has been proposed that a model-independent analysis based on ratioing and phase difference methods can be used to decouple the correlation between $\sigma - N$ and $R - c_3$, respectively [42,44,45,48,49]. In this approach, the amplitude and phase of the isolated first shell are

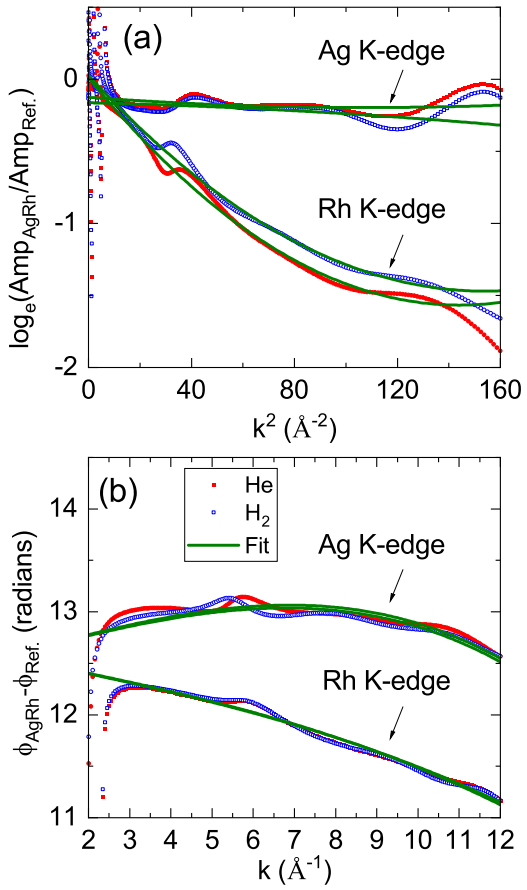

Fig. 4. Log-ratio fit (a) and phase difference fit (b) to the AgRh alloy NPs sample measured at the Ag and Rh K-edges under He and H_2 flows.

obtained by performing a backward Fourier transform of the χ(R) data. In the present case, the backward FT was performed on the reference data and those from the AgRh alloy NP sample. The transform range in R space was chosen to be between 1.3 and 3.3 Å for Rh and 1.6–3.6 Å for Ag covering the first shell and the Hanning window, with a sill width of 0.5. Fig. 4 shows plots of the indicated samples measured at the Ag and Rh K-edges. The logarithm of the amplitude ratios of the sample with the respective reference are plotted against k^2 in the Fig. 4(a) and the difference of the phases between the sample and reference is plotted against k in Fig. 4(b). Such a transformation is expected to give a straight line for systems free from any structural anharmonicity. By this approach, the coordination number and σ can be uncoupled, and these variables are respectively proportional to the intercept and slope in the amplitude ratio plots. Similarly, the slope of the curve in the phase difference plot measures the deviation in the atomic pair distance relative to the standard sample. Bunker [44] proposed that for samples having some degree of anharmonicity, the fitting of the amplitude ratio and the phase difference curve with the following equations can provide information on the relative variation in the parameters of the equation with respect to the standard.

$$Log - Ratio(k) = c_0 + 2c_2k^2 + \frac{2}{3}c_4k^4$$

$$Phase - Difference(k) = 2c_1k - \frac{4}{3}c_3k^3$$

In the above equations c_0, c_1, c_2, c_3, and c_4, are zero to fourth-order cumulants [49]. The obtained values of the fitting parameters are listed in Table 1. Here cumulants with $n \geq 2$ have a physical meaning with odd and even cumulants mainly affecting the phase and amplitude, respectively. Consequently, the first cumulant measures the relative change in the atomic pair distance and the second cumulant is σ. The third and fourth cumulants are used to measure the degree of anharmonicity in the sample. The value of the first cumulant (Table 1) for the sample measured at the Ag K-edge is negative and that for the sample measured at the Rh K-edge is positive. This result suggests that the atomic pair distance is shorter around Ag and longer around Rh relative to the respective standards, which is consistent with the XANES analysis. Moreover, the value of the third cumulant in the spectrum measured at the Rh K-edge is three times as great as that of the Ag K-edge. This result suggests that the effect of the third-order cumulant is higher for the spectra measured at the Rh K-edge. Therefore, we deduce that in the AgRh alloy NPs, the local environments of Rh and Ag are very different. The Rh environment has a considerable degree of anharmonicity relative to the Ag.

Table 1
Fitting results from ratioing analysis using Eqs. (1) and (2) for samples measured under a He flow.

Cumulants	Ag K-edge	Rh K-edge
c_0	−0.125(8)	0.026(8)
c_1	−0.0414(5)	0.0520(1)
c_2	0.0006(1)	0.0097(2)
c_3	0.000183(5)	0.00056(9)
c_4	0.000009(3)	0.00009(2)

After the above analysis, we derived the actual values of the metrical parameters by non-linear least-square fitting of the EXAFS data. The obtained metrical parameters are listed in Table S1, and the representative fitting plots are presented in Fig. S2. For the spectra measured at the Ag K-edge, initially, all the higher-order cumulants were excluded from the fitting, which gave a reasonably good fit. The obtained value of the atomic pair distance was found to be shorter than that of the standard. Any attempt to include higher-order cumulants in the fitting showed no improvement in the goodness of fit. The exclusion of higher-order cumulants from the Ag K-edge EXAFS fitting also corroborated with the ratioing analysis described above. The ratioing analysis demonstrated that the contribution from higher-order cumulants was less for Ag than for Rh. The EXAFS fitting of the alloy sample showed that the atomic pair distance for the first shell was smaller than that of the bulk. Moreover, the coordination number for the first shell is smaller indicating the presence of nanometer size clusters of the Ag.

Following a similar approach, we performed EXAFS fitting of the spectrum measured at the Rh K-edge. In the first approach, the cumulant was excluded from the fitting. By this approach, the atomic pair distance for the first shell was 2.68 Å which is similar to the value for bulk Rh. However, the XANES analysis, which is less sensitive to disorder, indicated that the atomic pair distance was slightly larger in the alloy sample than in the bulk. Hence, there is a correlation between the EXAFS phase with the third cumulant causing an underestimation of the atomic pair distance. Moreover, the aforementioned ratioing analysis confirms that higher-order cumulants have a greater contribution in the EXAFS measurements at the Rh K-edge. Consequently, the third cumulant is incorporated into the fitting of the first shell only, and for the rest of the shells, it was kept null. The inclusion of the third-order cumulant, yields an atomic pair distance that was slightly higher than that of the bulk (Table S1). A small correlation with ΔE_0 was also observed; however, the minimal variation had no measurable effect on the atomic pair distance. Including the fourth-order cumulant provided no major improvement in the fitting or any difference from the fitting parameters obtained after its exclusion. Therefore, only the effects of the third-order cumulant could be precisely assessed from the EXAFS data measured at the Rh K-edge. A slightly smaller first shell coordination number was observed for the EXAFS data measured at the Rh K-edge relative

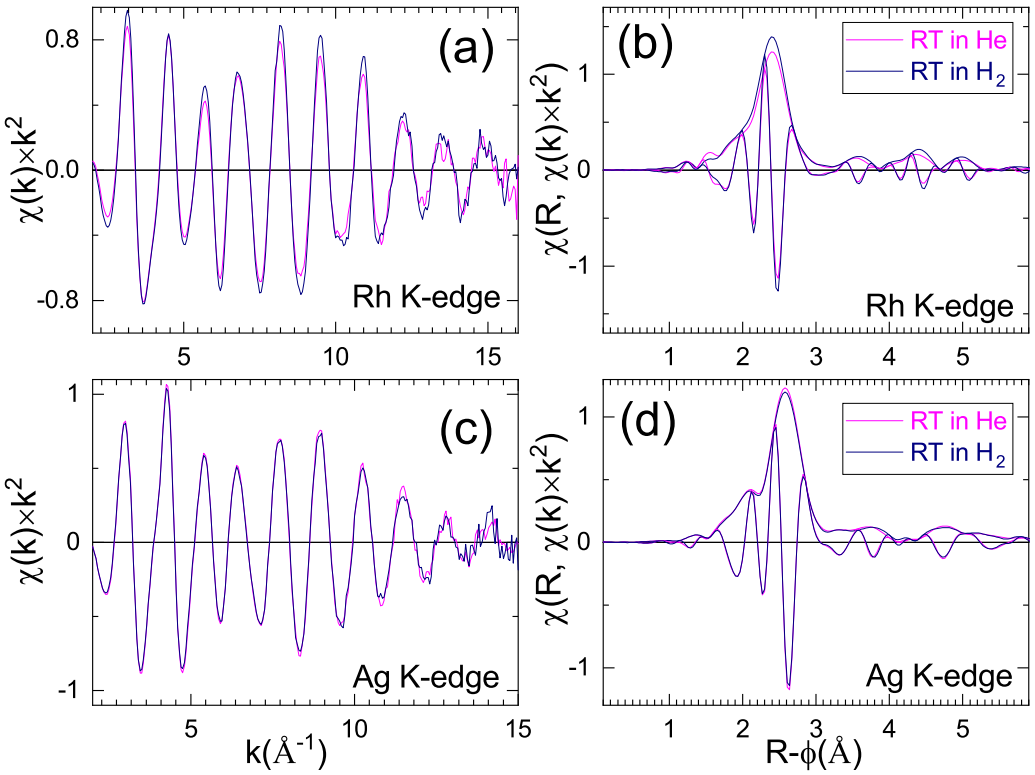

Fig. 5. EXAFS $\chi(k)k^2$ (a,c) and Fourier transform $\chi(R)$ (b,d) spectra of samples measured at the Rh K-edge (a,b) and Ag K-edge (c,d) under He or H_2 flow condition.

to the Ag K-edge, suggesting that the Rh clusters were smaller in size than the Ag clusters in the alloy sample.

Previous results for AgRh alloy NPs indicated suitability for the H_2 storage applications [21,22], although neither Ag nor Rh have H_2 solubility. Therefore, to understand the observed H_2 solubility in this NP alloy, we performed XAFS measurements under ambient temperature and pressure conditions with He (2 sccm) and H_2 (1.4 sccm) gas flows to investigate any variation in the local structure around Rh and Ag. Fig. 5 compares $\chi(k)$ (a,c) and the FT (b,d) spectra, and the metrical parameters derived from the EXAFS fitting are listed in Table S1. On comparing the FT and $\chi(k)$ spectra measured under the two gas flows, no noticeable changes in the variation of the atomic pair distance were observed (Table S1). Only slight variations in the FT and $\chi(k)$ amplitude were observed. Notably, the FT amplitude of the first peak at the Ag K-edge slightly decreased under the H_2 flow. In contrast, an alternative behavior was observed for the spectra measured at Rh K-edge. In comparing the amplitude of the $\chi(k)$ spectra, a slight decrease was observed for the Ag K-edge and the opposite behavior was seen for the Rh K-edge. Moreover, the change in the $\chi(k)$ amplitude was uniform over the entire k-region. Thus, the incorporation of H_2 induced slight growth in the particle size of Rh clusters and the opposite behavior for the Ag clusters was observed. Because the H_2 was flowed at a moderate rate (1.4 sccm) no major changes were expected. Moreover, Kusada et al. [21] reported that the hydrogen-to-metal ratio (H/M) for the equiatomic AgRh alloy is approximately 0.09, which is smaller than that of conventional Pd, and is capable of showing H/M between 0 and 1 [50]. Therefore, only marginal changes in the XAFS data are expected under the H_2 flow conditions.

Combining all the results obtained from XANES and EXAFS analysis of the samples measured under ambient, He, and H_2 flow conditions, we draw the following conclusions. Despite the formation of a solid-solution alloy, the local environments around Ag and Rh are distinct in the AgRh alloy NPs. The present XAFS analyses reveal that the formed solid-solution is a mixture of nano/sub-nanocrystalline Ag and Rh clusters, as schematically shown in Fig. S3. Bimetallic shells may be present in the metallic clusters but cannot be precisely evaluated owing to the limitations of XRD and XAFS. However, the atomic alloying in the interfacial region between the metal clusters have a notable effect on the local structure and reveals distinct local environments around both Rh and Ag. Substantial contributions from the structural anharmonicity are observed only around Rh. This result suggests that the Rh environment is significantly disordered than that of the Ag. Atomic-level mixing can take place; however, its contribution to the EXAFS signal is minimal. Nevertheless, the indirect effects of such mixing on the metal clusters in terms of significantly different atomic pair distances relative to the bulk can be seen. Therefore, atomically mixed alloys are mainly present in the proximity of the interfacial region. This interfacial region where atomic mixing occurs is important for governing the hydrogen absorption properties of the alloy owing to the possible emergence of unique electronic properties from hybridization of Ag and Rh electronic states. Moreover, this acts as a source of epitaxial strain that affects both the average long and short-range structure of nearby clusters. In the present case, under a H_2 flow, a slight increase in the coordination number around Rh was observed, accompanied by a small decrease in the coordination number around Ag. These results indicate that hydrogen is incorporated in the interfacial region resulting in variation of the cluster boundary stress, which results in the growth of the particle size of Rh and a small decrease in the Ag particle size. This effect is similar to that observed in pure nickel, where diffusion and trapping of hydrogen at grain boundary regions affects the grain size, grain boundary stress, and several other parameters [51,52]. These findings also indicate that the use of expensive Rh can be minimized by preparing alloyed samples that are mixed at the atomic level. In earlier investigations on PdPt core-shell NPs for hydrogen storage applications, the CS structure has been reported to transform to a solid solution phase with a greater degree of atomic-level mixing after the process of hydrogen absorption and desorption [53]. These

phenomena have been tested in other bimetallic systems. Furthermore, these findings indicate that in a wide range of immiscible bimetallic NPs, catalytic and chemical storage properties can be enhanced by the intelligent synthesis of the alloy structure. We propose that adopting a synthesis route that provides a higher fraction of atomically mixed alloy phase in the sample can markedly improve the performance of materials. Moreover, an understanding of the microstructure and electronic properties that emerge in the interfacial region of these novel bimetallic systems is important for tailoring of material systems to a variety of applications.

4. Conclusions

In conclusion, the microstructure and H_2 absorption properties of bulk immiscible AgRh alloy NPs were investigated. The XRD data of the alloy sample could be fitted by a single fcc structure. The value of the lattice parameter was obtained by Rietveld refinement. The value of the lattice parameter for the alloy sample was 4.015 ± 0.003 Å, which falls between the bulk value of Ag 4.08 Å and Rh 3.803 Å. XANES analysis revealed distinct local environments for Rh and Ag. In the Rh and Ag environments, the atomic pair distances were respectively larger and smaller than the bulk values. A notable fraction of the alloy phase formed via mixing of nano/sub-nano-sized clusters of Rh and Ag NPs. Mixing at the atomic level is likely possible at the interfacial region. The interfacial region plays an important role in propagating epitaxial strain affecting the microstructure of nearby NP clusters. Hydrogen absorption measurements performed under ambient conditions revealed that H_2 is mainly absorbed in the interfacial region where Ag and Rh form a perfect solid solution alloy.

CRediT authorship contribution statement

Akhil Tayal: Conceptualization, Methodology, Software, Validation, Formal analysis, Investigation, Data curation, Writing - original draft, Writing - review & editing, Visualization. **Okkyun Seo:** Conceptualization, Methodology, Software, Validation, Formal analysis, Investigation, Data curation, Writing - original draft, Writing - review & editing. **Jaemyung Kim:** Data curation. **Kohei Kusada:** Resources, Investigation, Data curation, Supervision, Conceptualization. **Hirokazu Kobayashi:** Resources, Investigation, Data curation, Supervision. **Hiroshi Kitagawa:** Funding acquisition, Project acquisition. **Osami Sakata:** Conceptualization, Methodology, Software, Validation, Formal analysis, Investigation, Data curation, Writing - original draft, Writing - review & editing, Supervision.

Declaration of Competing Interest

The authors declare that they have no known competing financial interests or personal relationships that could have appeared to influence the work reported in this paper.

Acknowledgements

The authors acknowledge Dr. Wolfgang Caliebe and Dr. Vadim Murzin for their help during the XAFS measurements. This project is partially funded by ACCEL (JPMJAC1501) and Japan Society for the Promotion of Science (JSPS) KAKENHI No. 18K04868 and 20K15083. We thank Andrew Jackson, Ph.D., from Edanz Group (https://en-author-services.edanzgroup.com/ac) for editing a draft of this manuscript.

Appendix A. Supporting information

Supplementary data associated with this article can be found in the online version at doi:10.1016/j.jallcom.2021.159268.

References

[1] S. Dekura, H. Kobayashi, K. Kusada, H. Kitagawa, Hydrogen in palladium and storage properties of related nanomaterials: size, shape, alloying, and metal-organic framework coating effects, ChemPhysChem 20 (2019) 1158–1176, https://doi.org/10.1002/cphc.201900109 ⟨https://onlinelibrary.wiley.com/doi/abs/⟩.
[2] N. Zheng, G.D. Stucky, A general synthetic strategy for oxide-supported metal nanoparticle catalysts, J. Am. Chem. Soc. 128 (2006) 14278–14280, https://doi.org/10.1021/ja0659929
[3] A.T. Gwathmey, R.E. Cunningham, The influence of crystal face in catalysis, Adv. Catal. 10 (1958) 57–95, https://doi.org/10.1016/S0360-0564(08)60404-6 ⟨http://www.sciencedirect.com/science/article/pii/S0360056408604046⟩.
[4] Y. Liu, H. Li, W. Cen, J. Li, Z. Wang, G. Henkelman, A computational study of supported Cu-based bimetallic nanoclusters for CO oxidation, Phys. Chem. Chem. Phys. 20 (2018) 7508–7513, https://doi.org/10.1039/C7CP08578H
[5] H. Li, G. Henkelman, Dehydrogenation selectivity of ethanol on close-packed transition metal surfaces: a computational study of monometallic, Pd/Au, and Rh/Au catalysts, J. Phys. Chem. C 121 (2017) 27504–27510, https://doi.org/10.1021/acs.jpcc.7b09953
[6] H. Li, L. Luo, P. Kunal, C.S. Bonifacio, Z. Duan, J.C. Yang, S.M. Humphrey, R.M. Crooks, G. Henkelman, Oxygen reduction reaction on classically immiscible bimetallics: a case study of RhAu, J. Phys. Chem. C 122 (2018) 2712–2716, https://doi.org/10.1021/acs.jpcc.7b10974
[7] S. García, L. Zhang, G.W. Piburn, G. Henkelman, S.M. Humphrey, Microwave synthesis of classically immiscible rhodium-silver and rhodium-gold alloy nanoparticles: highly active hydrogenation catalysts, ACS Nano 8 (2014) 11512–11521, https://doi.org/10.1021/nn504746u
[8] D. Wu, K. Kusada, H. Kitagawa, Recent progress in the structure control of Pd-Ru bimetallic nanomaterials, Sci. Technol. Adv. Mater. 17 (2016) 583–596, https://doi.org/10.1080/14686996.2016.1221727
[9] K. Sato, H. Tomonaga, T. Yamamoto, S. Matsumura, N.D.B. Zulkifli, T. Ishimoto, M. Koyama, K. Kusada, H. Kobayashi, H. Kitagawa, K. Nagaoka, A synthetic pseudo-Rh: NO_x reduction activity and electronic structure of Pd-Ru solid-solution alloy nanoparticles, Sci. Rep. 6 (2016) 28265, https://doi.org/10.1038/srep28265
[10] K. Kusada, H. Kobayashi, R. Ikeda, Y. Kubota, M. Takata, S. Toh, T. Yamamoto, S. Matsumura, N. Sumi, K. Sato, K. Nagaoka, H. Kitagawa, Solid solution alloy nanoparticles of immiscible Pd and Ru elements neighboring on Rh: changeover of the thermodynamic behavior for hydrogen storage and enhanced CO-oxidizing ability, J. Am. Chem. Soc. 136 (2014) 1864–1871, https://doi.org/10.1021/ja409464g
[11] G.P. Rachiero, U.B. Demirci, P. Miele, Bimetallic RuCo and RuCu catalysts supported on γ -Al_2O_3. a comparative study of their activity in hydrolysis of ammonia-borane, Int. J. Hydrog. Energy 36 (2011) 7051–7065, https://doi.org/10.1016/j.ijhydene.2011.03.009 ⟨http://www.sciencedirect.com/science/article/pii/S0360319911005970⟩.
[12] H. Nitani, T. Nakagawa, H. Daimon, Y. Kurobe, T. Ono, Y. Honda, A. Koizumi, S. Seino, T.A. Yamamoto, Methanol oxidation catalysis and substructure of PtRu bimetallic nanoparticles, Appl. Catal. A Gen. 326 (2007) 194–201, https://doi.org/10.1016/j.apcata.2007.04.018 ⟨http://www.sciencedirect.com/science/article/pii/S0926860×07002475⟩.
[13] J.-L. Mi, P. Nørby, M. Bremholm, J. Becker, B.B. Iversen, The formation mechanism of bimetallic PtRu alloy nanoparticles in solvothermal synthesis, Nanoscale 7 (2015) 16170–16174, https://doi.org/10.1039/C5NR04459F
[14] J. Suntivich, Z. Xu, C.E. Carlton, J. Kim, B. Han, S.W. Lee, N. Bonnet, N. Marzari, L.F. Allard, H.A. Gasteiger, K. Hamad-Schifferli, Y. Shao-Horn, Surface composition tuning of Au-Pt bimetallic nanoparticles for enhanced carbon monoxide and methanol electro-oxidation, J. Am. Chem. Soc. 135 (2013) 7985–7991, https://doi.org/10.1021/ja402072r
[15] Y. Zhao, C. Ye, W. Liu, R. Chen, X. Jiang, Tuning the composition of AuPt bimetallic nanoparticles for antibacterial application, Angew. Chem. Int. Ed. 53 (2014) 8127–8131, https://doi.org/10.1002/anie.201401035
[16] H. Zhang, N. Toshima, Fabrication of catalytically active AgAu bimetallic nanoparticles by physical mixture of small Au clusters with Ag ions, Appl. Catal. A Gen. 447–448 (2012) 81–88, https://doi.org/10.1016/j.apcata.2012.09.040 ⟨http://www.sciencedirect.com/science/article/pii/S0926860×12006333⟩.
[17] S. Divi, A. Chatterjee, Understanding segregation behavior in AuPt, NiPt, and AgAu bimetallic nanoparticles using distribution coefficients, J. Phys. Chem. C 120 (2016) 27296–27306, https://doi.org/10.1021/acs.jpcc.6b08325
[18] A. Kotsifa, T.I. Halkides, D.I. Konarides, X.E. Verykios, Activity enhancement of bimetallic Rh-Ag/Al_2O_3 catalysts for selective catalytic reduction of NO by C_3H_6, Catal. Lett. 79 (2002) 113–117, https://doi.org/10.1023/A:1015308408840
[19] K. Torigoe, H. Remita, P. Beaunier, J. Belloni, Radiation-induced reduction of mixed silver and rhodium ionic aqueous solution, Radiat. Phys. Chem. 64 (2002) 215–222, https://doi.org/10.1016/S0969-806X(01)00453-4 ⟨http://www.sciencedirect.com/science/article/pii/S0969806×01004534⟩.
[20] O. Inderwildi, S. Jenkins, D. King, When adding an unreactive metal enhances catalytic activity: NO_x decomposition over silver-rhodium bimetallic surfaces, Surf. Sci. 601 (2007) L103–L108, https://doi.org/10.1016/j.susc.2007.06.031 ⟨http://www.sciencedirect.com/science/article/pii/S0039602807006954⟩.
[21] K. Kusada, M. Yamauchi, H. Kobayashi, H. Kitagawa, Y. Kubota, Hydrogen-storage properties of solid-solution alloys of immiscible neighboring elements with Pd, J. Am. Chem. Soc. 132 (2010) 15896–15898, https://doi.org/10.1021/ja107362z
[22] A. Yang, O. Sakata, K. Kusada, T. Yayama, H. Yoshikawa, T. Ishimoto, M. Koyama, H. Kobayashi, H. Kitagawa, The valence band structure of Ag_xRh_{1-x} alloy nanoparticles, Appl. Phys. Lett. 105 (2014) 153109, https://doi.org/10.1063/1.4896857

[23] S. García, R.M. Anderson, H. Celio, N. Dahal, A. Dolocan, J. Zhou, S.M. Humphrey, Microwave synthesis of Au-Rh core-shell nanoparticles and implications of the shell thickness in hydrogenation catalysis, Chem. Commun. 49 (2013) 4241–4243, https://doi.org/10.1039/C3CC40387D
[24] C.S. Bonifacio, P. Kunal, H. Wan, S.M. Humphrey, J.C. Yang, Thermal stability study of classically immiscible Rh-Ag alloy nanoparticles by *in − situ* TEM, Microsc. Microanal. 22 (2016) 820–821, https://doi.org/10.1017/S1431927616004955
[25] P. Kunal, E.J. Roberts, C.T. Riche, K. Jarvis, N. Malmstadt, R.L. Brutchey, S.M. Humphrey, Continuous flow synthesis of Rh and RhAg alloy nanoparticle catalysts enables scalable production and improved morphological control, Chem. Mater. 29 (2017) 4341–4350, https://doi.org/10.1021/acs.chemmater.7b00694
[26] J.V. Pande, A.B. Bindwal, Y.B. Pakade, R.B. Biniwale, Application of microwave synthesized Ag-Rh nanoparticles in cyclohexane dehydrogenation for enhanced H_2 delivery, Int. J. Hydrog. Energy 43 (2018) 7411–7423, https://doi.org/10.1016/j.ijhydene.2018.02.105 ⟨http://www.sciencedirect.com/science/article/pii/S036031991830572X⟩.
[27] K. Kusada, D. Wu, T. Yamamoto, T. Toriyama, S. Matsumura, W. Xie, M. Koyama, S. Kawaguchi, Y. Kubota, H. Kitagawa, Emergence of high ORR activity through controlling local density-of-states by alloying immiscible Au and Ir, Chem. Sci. 10 (2019) 652–656, https://doi.org/10.1039/C8SC04135K
[28] Q. Zhang, K. Kusada, D. Wu, N. Ogiwara, T. Yamamoto, T. Toriyama, S. Matsumura, S. Kawaguchi, Y. Kubota, T. Honma, H. Kitagawa, Solid-solution alloy nanoparticles of a combination of immiscible Au and Ru with a large gap of reduction potential and their enhanced oxygen evolution reaction performance, Chem. Sci. 10 (2019) 5133–5137, https://doi.org/10.1039/C9SC00496C
[29] S. Xiao, W. Hu, W. Luo, Y. Wu, X. Li, H. Deng, Size effect on alloying ability and phase stability of immiscible bimetallic nanoparticles, Eur. Phys. J. B Condens. Matter Complex Syst. 54 (2006) 479–484, https://doi.org/10.1140/epjb/e2007-00018-6
[30] Y. Shubin, P. Plyusnin, M. Sharafutdinov, E. Makotchenko, S. Korenev, Successful synthesis and thermal stability of immiscible metal Au-Rh, Au-Ir and Au-Ir-Rh nanoalloys, Nanotechnology 28 (2017) 205302, https://doi.org/10.1088/1361-6528/aa6bc9
[31] A. Obuchi, A. Ohi, M. Nakamura, A. Ogata, K. Mizuno, H. Ohuchi, Performance of platinum-group metal catalysts for the selective reduction of nitrogen oxides by hydrocarbons, Appl. Catal. B Environ. 2 (1993) 71–80, https://doi.org/10.1016/0926-3373(93)80027-B ⟨http://www.sciencedirect.com/science/article/pii/092633739380027B⟩.
[32] G.R. Bamwenda, A. Ogata, A. Obuchi, J. Oi, K. Mizuno, J. Skrzypek, Selective reduction of nitric oxide with propene over platinum-group based catalysts: studies of surface species and catalytic activity, Appl. Catal. B Environ. 6 (1995) 311–323, https://doi.org/10.1016/0926-3373(95)00020-8 ⟨http://www.sciencedirect.com/science/article/pii/0926337395000208⟩.
[33] D.-H. Seo, H. Shin, K. Kang, H. Kim, S.S. Han, First-principles design of hydrogen dissociation catalysts based on isoelectronic metal solid solutions, J. Phys. Chem. Lett. 5 (2014) 1819–1824, https://doi.org/10.1021/jz500496e
[34] W.A. Caliebe, V. Murzin, A. Kalinko, M. Görlitz, High-flux XAFS-beamline P64 at PETRA III, AIP Conf. Proc. 2054 (2019) 060031, https://doi.org/10.1063/1.5084662
[35] B. Ravel, M. Newville, *ATHENA*, *ARTEMIS*, *HEPHAESTUS*: data analysis for X-ray absorption spectroscopy using *IFEFFIT*, J. Synchrotron Radiat. 12 (2005) 537–541, https://doi.org/10.1107/S0909049505012719
[36] S.D. Conradson, T. Durakiewicz, F.J. Espinosa-Faller, Y.Q. An, D.A. Andersson, A.R. Bishop, K.S. Boland, J.A. Bradley, D.D. Byler, D.L. Clark, D.R. Conradson, L.L. Conradson, A.L. Costello, N.J. Hess, G.H. Lander, A. Llobet, M.B. Martucci, J. Mustre de Leon, D. Nordlund, J.S. Lezama-Pacheco, T.E. Proffen, G. Rodriguez, D.E. Schwarz, G.T. Seidler, A.J. Taylor, S.A. Trugman, T.A. Tyson, J.A. Valdez, Possible Bose-condensate behavior in a quantum phase originating in a collective excitation in the chemically and optically doped Mott-Hubbard system UO_{2-x}, Phys. Rev. B 88 (2013) 115135, https://doi.org/10.1103/PhysRevB.88.115135
[37] J.J. Rehr, J.J. Kas, F.D. Vila, M.P. Prange, K. Jorissen, Parameter-free calculations of x-ray spectra with feff9, Phys. Chem. Chem. Phys. 12 (2010) 5503–5513, https://doi.org/10.1039/B926434E
[38] V.O. Kostroun, R.W. Fairchild, C.A. Kukkonen, J.W. Wilkins, Systematic structure in the *k* -edge photoabsorption spectra of the 4*d* transition metals, Phys. Rev. B 13 (1976) 3268–3271, https://doi.org/10.1103/PhysRevB.13.3268
[39] J.E. Muller, O. Jepsen, O.K. Andersen, J.W. Wilkins, Systematic structure in the *k* -edge photoabsorption spectra of the 4*d* transition metals: theory, Phys. Rev. Lett. 40 (1978) 720–722, https://doi.org/10.1103/PhysRevLett.40.720
[40] G.S. Hendereson, F.M.d. Groot, B.J. Moulton, X-ray absorption near-edge structure (XANES) spectroscopy, Rev. Mineral. Geochem. 78 (2014) 75–138, https://doi.org/10.2138/rmg.2014.78.3
[41] A.I. Frenkel, C.W. Hills, R.G. Nuzzo, A view from the inside: complexity in the atomic scale ordering of supported metal nanoparticles, J. Phys. Chem. B 105 (2001) 12689–12703, https://doi.org/10.1021/jp012769j
[42] A.I. Frenkel, A. Yevick, C. Cooper, R. Vasic, Modeling the structure and composition of nanoparticles by extended x-ray absorption fine-structure spectroscopy, Annu. Rev. Anal. Chem. 4 (2011) 23–39, https://doi.org/10.1146/annurev-anchem-061010-113906 ⟨https://www.ncbi.nlm.nih.gov/pubmed/21351882⟩.
[43] N. Marinkovic, K. Sasaki, R. Adzic, Nanoparticle size evaluation of catalysts by EXAFS: advantages and limitations, Zaštita Mater. 57 (2016) 101–109, https://doi.org/10.5937/ZasMat1601101M
[44] G. Bunker, Application of the ratio method of EXAFS analysis to disordered systems, Nucl. Instrum. Methods Phys. Res. 207 (1983) 437–444, https://doi.org/10.1016/0167-5087(83)90655-5 ⟨http://www.sciencedirect.com/science/article/pii/0167508783906555⟩.
[45] B.S. Clausen, J.K. Nørskov, Asymmetric pair distribution functions in catalysts, Top. Catal. 10 (2000) 221–230, https://doi.org/10.1023/A:1019196908404
[46] A. Manceau, P. Bustamante, A. Haouz, J.P. Bourdineaud, M. Gonzalez-Rey, C. Lemouchi, I. Gautier-Luneau, V. Geertsen, E. Barruet, M. Rovezzi, P. Glatzel, S. Pin, Mercury(II) binding to metallothionein in Mytilus edulis revealed by high energy-resolution XANES spectroscopy, Chem. A Eur. J. 25 (2019) 997–1009, https://doi.org/10.1002/chem.201804209
[47] J.E. Penner-Hahn, Characterization of “spectroscopically quiet” metals in biology, Coord. Chem. Rev. 249 (2005) 161–177, https://doi.org/10.1016/j.ccr.2004.03.011 ⟨http://www.sciencedirect.com/science/article/pii/S001085450400058X⟩.
[48] F. Farges, G.E. Brown, P.-E. Petit, M. Munoz, Transition elements in water-bearing silicate glasses/melts. part i. a high-resolution and anharmonic analysis of Ni coordination environments in crystals, glasses, and melts, Geochim. Cosmochim. Acta 65 (2001) 1665–1678, https://doi.org/10.1016/S0016-7037(00)00625-6 ⟨http://www.sciencedirect.com/science/article/pii/S0016703700006256⟩.
[49] S. Calvin, XAFS for Everyone, CRC Press, 2013.
[50] J.D. Benck, A. Jackson, D. Young, D. Rettenwander, Y.-M. Chiang, Producing high concentrations of hydrogen in palladium via electrochemical insertion from aqueous and solid electrolytes, Chem. Mater. 31 (2019) 4234–4245, https://doi.org/10.1021/acs.chemmater.9b01243
[51] A. Oudriss, J. Creus, J. Bouhattate, E. Conforto, C. Berziou, C. Savall, X. Feaugas, Grain size and grain-boundary effects on diffusion and trapping of hydrogen in pure nickel, Acta Mater. 60 (2012) 6814–6828, https://doi.org/10.1016/j.actamat.2012.09.004 ⟨http://www.sciencedirect.com/science/article/pii/S1359645412006106⟩.
[52] A. Pundt, Hydrogen in nano-sized metals, Adv. Eng. Mater. 6 (2004) 11–21, https://doi.org/10.1002/adem.200300557
[53] A. Tayal, O. Seo, J. Kim, L.S.R. Kumara, C. Song, S. Hiroi, Y. Chen, H. Kobayashi, H. Kitagawa, O. Sakata, Effects of interfacial structure of Pd-Pt nanoparticles on hydrogen solubility, J. Alloy. Compd. 791 (2019) 1263–1269, https://doi.org/10.1016/j.jallcom.2019.03.342 ⟨http://www.sciencedirect.com/science/article/pii/S0925838819311806⟩.